

# Transport through a quantum ring, a dot and a barrier embedded in a nanowire in magnetic field

Vidar Gudmundsson,<sup>1</sup> Yu-Yu Lin,<sup>2</sup> Chi-Shung Tang,<sup>3</sup> Valeriu Moldoveanu,<sup>4</sup> Jens Hjorleifur Bardarson,<sup>1</sup> and Andrei Manolescu<sup>1,4</sup>

<sup>1</sup>*Science Institute, University of Iceland, Dunhaga 3, IS-107 Reykjavik, Iceland*

<sup>2</sup>*Department of Electrophysics, National Chiao Tung University, Hsinchu 30010, Taiwan*

<sup>3</sup>*Physics Division, National Center for Theoretical Sciences, P.O. Box 2-131, Hsinchu 30013, Taiwan*

<sup>4</sup>*Institute of Physics and Technology of Materials, P.O. Box MG7, Bucharest-Magurele, Romania*

We investigate the transport through a quantum ring, a dot and a barrier embedded in a nanowire in a homogeneous perpendicular magnetic field. To be able to treat scattering potentials of finite extent in magnetic field we use a mixed momentum-coordinate representation to obtain an integral equation for the multiband scattering matrix. For a large embedded quantum ring we are able to obtain Aharonov-Bohm type of oscillations with superimposed narrow resonances caused by interaction with quasi-bound states in the ring. We also employ scattering matrix approach to calculate the conductance through a semi-extended barrier or well in the wire. The numerical implementations we resort to in order to describe the cases of weak and intermediate magnetic field allow us to produce high resolution maps of the “near field” scattering wave functions, which are used to shed light on the underlying scattering processes.

## I. INTRODUCTION

The influence of a single impurity on the conductance of a quasi one-dimensional quantum channel has been investigated by several groups theoretically<sup>1,2,3,4</sup> and experimentally.<sup>5</sup> Commonly the impurities are considered to be short range and represented by a  $\delta$ -function, though treatments of more extended scatterers, like square barriers,<sup>2</sup> can be found. Recently, the application to nanosized systems, has spurred the use of general methods built on the Lippmann-Schwinger equation or the equivalent  $T$ -matrix formalism to describe the scattering of more general extended potentials in quantum channels<sup>6</sup> or curved wires.<sup>7</sup>

The inclusion of a constant homogeneous magnetic field perpendicular to the quasi one-dimensional electron channel or wire drastically changes the properties of the system. Without the magnetic field a centered symmetric scattering potential leads to “selection rules” that restrict the possible scattering processes. These are lifted by the magnetic field resulting in a rich structure contrasted to the conductance steps in an ideal wire as long as the magnetic length is not much shorter than the width of the wire and the range of the scattering potential.<sup>8</sup>

The character of the Lorentz force does not allow us to establish a simple multimode formulation of the scattering process in configuration space,<sup>4</sup> but in strong magnetic field Gurvitz used a scheme to develop a multimode formalism using a Fourier Transform with respect to the transport direction, and a truncation to a two-mode formalism allowed him to seek analytical solutions for a short range scatterer present in a wire with general confinement.<sup>9</sup>

Here we extend this formalism by noting that in the case of a parabolic shape of the wire confinement we obtain coupled Lippmann-Schwinger equations with a non-local scattering potential in Fourier space for the different

modes. A transformation of this system of equations to corresponding equations for the  $T$ -matrix shows that it bears a strong resemblance to the corresponding equations for the system in no external magnetic field.<sup>6</sup> We exploit this fact to seek numerical solutions for the system in weak and intermediate strength of the magnetic field where a two mode approximation is not always warranted. One benefit of the numerical approach is that it allows us to map out with high resolution the probability density for the scattering states near the scatterer. These “near field” solutions give us a good indication of the scattering process itself. We explore a quantum wire with an embedded quantum dot or a ring. We are able to increase the size of the ring to the limit that we observe Aharonov-Bohm type of oscillations.

In order to investigate the scattering of potentials that are homogeneous in the direction perpendicular to the wire representing a barrier or a well we employ an alternative method based on mode matching. The smooth scattering potential is sliced into a series of  $\delta$ -potentials. The scattering matrix is then constructed from repeated mode matching at each slice.

## II. MODELS

We consider electron transport along a parabolically confined quantum wire parallel to the  $x$ -axis and perpendicular to a homogeneous magnetic field  $\mathbf{B} = B\hat{\mathbf{z}}$ . In the center of the wire the electrons are scattered by a potential  $V_{sc}(\mathbf{r})$  to be specified below. The system under investigation is described by the Hamiltonian  $H = H_0 + V_{sc}(\mathbf{r})$  with

$$H_0 = \frac{\hbar^2}{2m^*} \left[ -i\mathbf{\nabla} - \frac{eB}{\hbar c} y\hat{\mathbf{x}} \right]^2 + V_c(y), \quad (1)$$

where the wire is assumed to be parabolically confined, namely  $V_c(y) = m^* \Omega_0^2 y^2 / 2$  with  $m^*$  and  $\Omega_0$  being, respectively, the effective mass of an electron in GaAs-based material and the confinement parameter. Here  $-e$  is the charge of an electron. We present two quite different approaches to describe the scattering process of incoming electron states, one using wave function matching appropriate to describe scattering from a thin homogeneous barrier or well perpendicular the wire, and the other one using a  $T$ -matrix formalism to calculate the scattering of an embedded quantum dot or ring in the wire.

### A. Scattering matrix approach

In this section, we employ the scattering matrix approach to the calculation of coherent electronic transport in a quantum wire in the presence of a Gaussian-profile scattering potential. The potential under investigation can be realized as a finger gate atop the wire and can be modeled by

$$V_{sc}(\mathbf{r}) = V_0 \exp(-\beta x^2), \quad (2)$$

as is shown in Fig. 1.

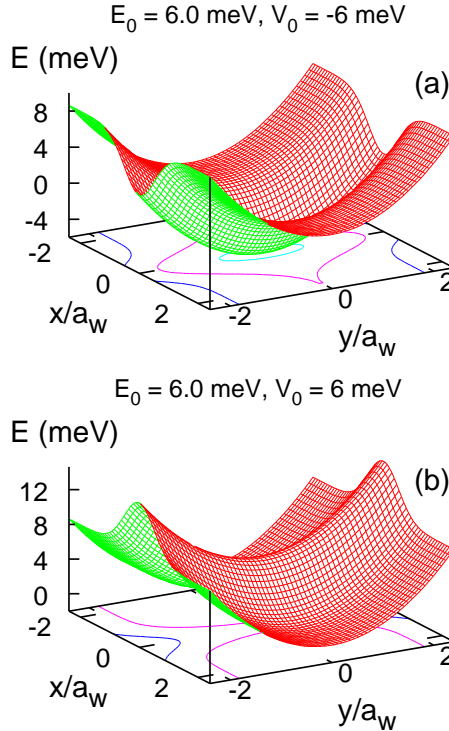


FIG. 1: Barrier or well embedded in a quantum wire with  $V_0 =$  (a)  $-6$  meV and (b)  $6$  meV, respectively. Other parameters are  $B = 0$  T,  $a_w = 33.7$  nm,  $E_0 = \hbar\Omega_0 = 6.0$  meV, and  $\beta a_w^2 = 1.897$ .

To obtain a dimensionless expression we employ the Bohr radius  $a_0$ , and have thus the relevant units for the

confinement parameter  $\Omega_0^* = \hbar/(m^* a_0^2)$ , and the magnetic field  $B^* = \hbar c/(e a_0^2)$ . As such, by defining the unit of the cyclotron frequency to be  $\omega_c^* = \Omega_0^*$ , the cyclotron frequency simply has the dimensionless form  $\omega_c = B$ .

In the absence of scatterers the eigenfunctions of  $H_0$  can be written as<sup>9</sup>

$$\psi^\pm(x, y, k_n) = e^{\pm i k_n x} \chi^\pm(y, k_n) \quad (3)$$

with  $\pm k_n$  being the wave vector along  $\pm \hat{x}$  in the  $n$ th transverse subband, where  $\chi^\pm(y, k_n)$  satisfies the reduced dimensionless equation

$$\left[ -\frac{\partial^2}{\partial y^2} + \Omega_w^2 (y \mp \alpha_n)^2 \right] \chi^\pm(y, k_n) = E_n \chi^\pm(y, k_n), \quad (4)$$

which is a harmonic oscillator of frequency  $\Omega_w$  with a shifted center  $\alpha_n = \omega_c k_n / \Omega_w^2$ . These eigenmodes of the electron in a state described by  $\psi(x, y, k_n)$  in a pure quantum wire have the energy spectrum

$$E = E_n + \mathcal{K}(k_n), \quad (5)$$

composed of Landau levels  $E_n = (n + 1/2) \Omega_w$ , where  $\Omega_w = \sqrt{\omega_c^2 + \Omega_0^2}$ , shifted by the confining potential, and the kinetic energy  $\mathcal{K}(k_n) = k_n^2 (\Omega_0 / \Omega_w)^2$ . The eigenfunctions  $\chi^\pm(y, k_n)$  of the eigenmodes are given by

$$\chi^\pm(y, k_n) = N_n H_n \left[ \sqrt{\Omega_w} (y \mp \alpha_n) \right] \exp \left[ -\frac{\Omega_w}{2} (y \mp \alpha_n)^2 \right], \quad (6)$$

where  $N_n = (\Omega_w / \pi)^{1/4} (2^n n!)^{-1/2}$  is a normalization constant.

To utilize the scattering matrix approach, we divide the Gaussian scattering potential into a series of slices of width  $\delta L$ , each of them is described by a delta-profile potential

$$V_{sc}(x_i) = V_0 \delta L \exp(-\beta x_i^2) \delta(x - x_i). \quad (7)$$

The Gaussian potential Eq. (2) can thus be described by  $V_{sc}(\mathbf{r}) = \sum_{i=1}^{N_L} V_{sc}(x_i)$  if we divide the potential into sufficiently many pieces. For a right-going incident wave  $\psi(x, y, k_n)$  from the  $n$ th mode of the left reservoir, the corresponding scattering wave function can be expressed in the form

$$\begin{aligned} \psi_n^{(i)}(x, y, k_n) = & e^{i k_n x} \chi_n^+(y, k_n) \\ & + \sum_{n'} r_{n'n}^i e^{-i k_{n'} x} \chi_{n'}^-(y, k_{n'}) \end{aligned} \quad (8)$$

for  $x < x_i$ , and

$$\psi_n^{(i)}(x, y, k_n) = \sum_{n'} t_{n'n}^i e^{-i k_{n'} x} \chi_{n'}^+(y, k_{n'}) \quad (9)$$

for  $x > x_i$ . Following similar procedure we can also obtain the reflection and transmission coefficients,  $\tilde{r}_{n'n}^i$  and  $\tilde{t}_{n'n}^i$ , for a left-going incident wave.

The scattering should satisfy two boundary conditions, one requirement is that  $\psi(x, y)$  has to be continuous at  $x = x_i$  and the other one stems from integration of the Schrödinger equation across  $x = x_i$ . Multiplying these boundary conditions by the eigenfunction  $\chi_m(y)$  of the ordinary unshifted harmonic oscillator with confining frequency  $\Omega_w$ , and integrating over  $y$ , we obtain

$$\sum_{n'} I_{mn'}^+(k_{n'}) t_{n'n}^i - \sum_{n'} I_{mn'}^-(k_{n'}) r_{n'n}^i = I_{mn}^+(k_n) \quad (10)$$

$$\sum_{n'} J_{mn'}^+(k_{n'}) t_{n'n}^i + \sum_{n'} K_{mn'}^-(k_{n'}) r_{n'n}^i = k_n I_{mn}^+(k_n) \quad (11)$$

where the matrix elements are related to the overlap integrals

$$I_{mn'}^\pm = \int \chi_m(y) \chi_{n'}^\pm(y) dy, \quad (12)$$

$$J_{mn'}^+(k_{n'}) = k_{n'} I_{mn'}^+(k_{n'}) + i V_0 V_{mn'}^+ \quad (13)$$

with

$$V_{mn'}^+ = \int \chi_m(y) V_{sc}(y) \chi_{n'}^\pm(y) dy, \quad (14)$$

and

$$K_{mn'}^-(k_{n'}) = k_{n'} I_{mn'}^-(k_{n'}). \quad (15)$$

Using Eqs. (10)-(11) and the corresponding equations for  $\tilde{r}_{n'n}^i$  and  $\tilde{t}_{n'n}^i$ , one can establish the scattering matrix for the Gaussian-shape potential.<sup>10</sup> From the ratio of the transmitted and the incident current we obtain the current transmission  $T_{\beta\alpha}$ , in which  $\alpha$  and  $\beta$  are, respectively, the incident and the transmitting lead. Since the current flowing into the terminal  $R$  (drain) from the system should take into account the current into the terminal  $L$  (source) from the system, the net charge current into terminal  $R$  is therefore given by

$$I(V) = \frac{2e}{h} \int_0^{\mu+eV/2} dE f_L(E) T_{RL}(E) - \frac{2e}{h} \int_0^{\mu-eV/2} dE f_R(E) T_{LR}(E) \quad (16)$$

where  $f(E)$  indicates the Fermi distribution function and  $\mu$  is the zero-bias Fermi level. The two-terminal conductance is given by  $G = \partial I / \partial V$ . Below we assume that the scattering potential is located at the center of the nanowire, the applied perpendicular magnetic field is homogeneous, and the source-drain bias is sufficiently low. Hence, the zero temperature conductance can be

expressed in terms of the incident electron energy  $E$  in the simple form

$$G(E) = \frac{2e^2}{h} \sum_{n=0}^N T_n(E), \quad (17)$$

where  $N$  denotes the highest propagating mode incident from the source electrode. The current transmission coefficient  $T_n(E)$  for an electron incident in the  $n$ th subband from the source electrode is given by

$$T_n(E) = \sum_{n'(\mu_{n'} > 0)} \frac{k_{n'}}{k_n} |t_{n'n}^{RL}|^2. \quad (18)$$

The current reflection coefficient  $R_n(E)$  can be calculated by a similar form to get current conservation condition for checking the numerical accuracy.

## B. T-matrix formalism

We consider a quantum dot or a ring embedded in the wire and parameterize the scattering potential accordingly combining two Gaussian functions of different shapes

$$V_{sc}(\mathbf{r}) = V_1 \exp(-\beta_1 r^2) + V_2 \exp(-\beta_2 r^2), \quad (19)$$

as is shown in Fig. 2. Together the magnetic field and the parabolic confinement define a natural length scale  $a_w = \sqrt{\hbar/(m^*)\Omega_w}$ , where  $\Omega_w = \sqrt{\omega_c^2 + \Omega_0^2}$ , with the cyclotron frequency  $\omega_c = eB/(m^*c)$ , is the natural frequency of the quantum wire in a magnetic field.

Along the lines of Gurvitz we choose to use the mixed momentum-coordinate presentation of the wave functions<sup>9</sup>

$$\Psi_E(p, y) = \int dx \psi_E(x, y) e^{-ipx}, \quad (20)$$

and expand them in channel modes

$$\Psi_E(p, y) = \sum_n \varphi_n(p) \phi_n(p, y), \quad (21)$$

i.e. in terms of the eigenfunctions for the pure parabolically confined wire in magnetic field

$$\phi_n(p, y) = \frac{\exp[-\frac{1}{2}(\frac{y-y_0}{a_w})^2]}{\sqrt{2^n} \sqrt{\pi n!} a_w} H_n\left(\frac{y-y_0}{a_w}\right), \quad (22)$$

with the center coordinate  $y_0 = p a_w^2 \omega_c / \Omega_w$ . These eigenmodes of the pure quantum wire have the energy spectrum  $E_{np} = E_n + \kappa_n(p)$  with  $E_n = \hbar \Omega_w (n + 1/2)$  and

$$\kappa_n(p) = \frac{(p a_w)^2}{2} \frac{(\hbar \Omega_0)^2}{\hbar \Omega_w}. \quad (23)$$

Using Eq.'s (20-23) and performing a Fourier transform with respect to the coordinate  $x$  transforms the

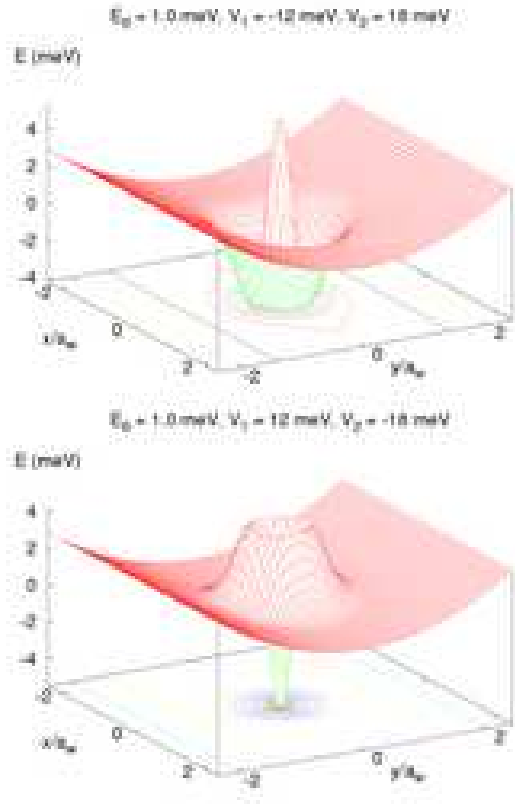


FIG. 2: Quantum ring (upper) or dot (lower) embedded in a quantum wire,  $B = 0$  T,  $a_w = 33.7$  nm,  $E_0 = \hbar\Omega_0 = 1.0$  meV,  $\beta_1 a_w^2 = 3.41$ , and  $\beta_2 a_w^2 = 11.37$ .

Schrödinger equation corresponding to the Hamiltonian (1) into a system of coupled nonlocal integral equations in momentum space

$$\kappa_n(q)\varphi_n(q) + \sum_{n'} \int \frac{dp}{2\pi} V_{nn'}(q, p)\varphi_{n'}(p) = (E - E_n)\varphi_n(q), \quad (24)$$

where

$$V_{nn'}(q, p) = \int dy \phi_n^*(q, y) V(q - p, y) \phi_{n'}(p, y), \quad (25)$$

and

$$V(q - p, y) = \int dx e^{-i(q-p)x} V_{sc}(x, y). \quad (26)$$

The matrix elements (25-26) for the scattering potential (19) can be evaluated analytically since they consist of Gaussians and Hermite polynomials, see Appendix A.

The special form of the part of the energy dispersion  $\kappa_n(q)$  for parabolic confinement allows us now to rewrite Eq. (24) as

$$\begin{aligned} &[-(qa_w)^2 + (k_n(E)a_w)^2]\varphi_n(q) \\ &= \frac{2\hbar\Omega_w}{(\hbar\Omega_0)^2} \sum_{n'} \int \frac{dp}{2\pi} V_{nn'}(q, p)\varphi_{n'}(p), \end{aligned} \quad (27)$$

where we have defined the effective band momentum  $k_n(E)$  as

$$(E - E_n) = \frac{[k_n(E)]^2}{2} \frac{(\hbar\Omega_0)^2}{\hbar\Omega_w}. \quad (28)$$

In the absence of a magnetic field it is possible to derive an equivalent effective one-dimensional multi-band Schrödinger equation to (27) in configuration space.<sup>4</sup> This multi-band equation is then usually transformed into a system of effective one-dimensional coupled Lippmann-Schwinger integral equations that is convenient for numerical computation. Here we can proceed along these lines, but the magnetic field forces us to do this in momentum space where we shall see that the corresponding Lippmann-Schwinger equations are better transformed into integral equations for the  $T$ -matrix in order to facilitate numerical evaluation. Considering Eq. (27) it is clear that the incoming scattering states satisfy

$$[-(qa_w)^2 + (k_n(E)a_w)^2] \varphi_n^0(q) = 0, \quad (29)$$

which implies a Greens function

$$[-(qa_w)^2 + (k_n(E)a_w)^2] G_E^n(q) = 1. \quad (30)$$

The Greens function can now be used to write down coupled Lippmann-Schwinger equations in momentum space

$$\varphi_n(q) = \varphi_n^0(q) + G_E^n(q) \sum_{n'} \int \frac{dpa_w}{2\pi} \tilde{V}_{nn'}(q, p) \varphi_{n'}(p), \quad (31)$$

where  $\tilde{V}_{nn'}(q, p) = V_{nn'}(q, p)2\hbar\Omega_w/[a_w(\hbar\Omega_0)^2]$ . These equations are inconvenient for numerical evaluation as the in-state  $\varphi_n^0$  is proportional to a Dirac delta function. Symbolically Eq. (31) can be expressed as  $\varphi = \varphi^0 + G\tilde{V}\varphi$ , and an iteration of the equation gives  $\varphi = \varphi^0 + G\tilde{V}\varphi^0 + G\tilde{V}G\tilde{V}\varphi^0 + \dots = (1 + G\tilde{T})\varphi^0$ , where we have introduced the  $T$ -matrix satisfying the symbolic equation  $\tilde{T} = \tilde{V} + \tilde{V}G\tilde{T}$ . Fully written the equation determining the  $T$ -matrix is

$$\begin{aligned} \tilde{T}_{nn'}(q, p) = &\tilde{V}_{nn'}(q, p) \\ &+ \sum_{m'} \int \frac{dk a_w}{2\pi} \tilde{V}_{nm'}(q, k) G_E^{m'}(k) \tilde{T}_{nm'}(k, p). \end{aligned} \quad (32)$$

This set of equations is easier to solve numerically than the equivalent Lippmann-Schwinger equations (31) after the singularities of the Greens function have been handled with special care.<sup>11</sup> We obtain analytically the contribution of the poles of the Greens function and perform the remaining principal part integration by removing the singularity by a subtraction of a zero.<sup>12,13</sup>

Comparison with the nonseparable two-dimensional Lippmann-Schwinger equation in configuration space for extended scattering potential in a magnetic field gives the connection between the  $T$ -matrix and the probability

amplitude for transmission in mode  $n$  with momentum  $k_n$  if the in-state is in mode  $m$  with momentum  $k_m$

$$t_{nm}(E) = \delta_{nm} - \frac{i\sqrt{(k_m/k_n)}}{2(k_m a_w)} \left( \frac{\hbar\Omega_0}{\hbar\Omega_w} \right)^2 \tilde{T}_{nm}(k_n, k_m). \quad (33)$$

The conductance is then according to the Landauer-Büttiker formalism defined as

$$G(E) = \frac{2e^2}{h} \text{Tr}[\mathbf{t}^\dagger(E)\mathbf{t}(E)], \quad (34)$$

where  $\mathbf{t}$  is evaluated at the Fermi energy.

Symbolically the wave function can be expressed as  $\varphi = (1 + GT)\varphi^0$  if the in-state  $\varphi^0$  is given. Together with Eq. (20) and (21) this gives

$$\begin{aligned} \psi_E(x, y) = & e^{ik_n x} \phi_n(k_n, y) \\ & + \sum_m \int \frac{dq a_w}{2\pi} e^{iqx} G_E^m(q) \tilde{T}_{mn}(q, k_n) \phi_m(q, y), \end{aligned} \quad (35)$$

for an incident electron with energy  $E$ , in mode  $n$  with momentum  $k_n$ . To calculate the wave function the same methods are used to isolate the contribution from the poles of the Greens function as were used for the calculation of  $\tilde{T}$  with Eq. (32).

### III. RESULTS

#### A. Embedded barrier

In this section, we present our numerical results of exploring electronic transport properties using a Gaussian-shape potential model described by Eq. (2) – the conductance versus the incident electron energy  $E$ . The parameters used to obtain our numerical results are taken from the GaAs-Al<sub>x</sub>Ga<sub>1-x</sub>As heterostructure system. The values that we choose for our material parameters are  $E_{\text{Ryd}} = 5.93$  meV and  $a_0 = 9.79$  nm.

The conductance Eq. (17) of the wire is presented in Fig. 3 for several values of magnetic field. To explore the transport properties it is convenient to show the conductance as a function of energy of the incoming electron state scaled by the subband energy level spacing  $X = E/\hbar\Omega_w + 1/2$  such that the integral values of  $X$  indicates the number of incident modes. In Fig. 3, we present the conductance for magnetic fields with strengths from 0 to 2.4 T for either weak ( $V_0 = -6$  meV) or strong ( $V_0 = -12$  meV) attractive potentials, as shown in Fig. 3(a) and (b), respectively. For the case of weak attractive potential shown in Fig. 3(a), one can see that the dip structures in  $G(E)$  are pinned at around  $X \simeq n + 0.85$ , and the location is insensitive to the magnetic field. It turns out that these structures correspond to the electrons incident from subband  $n$  scattered elastically into the  $n + 1$  subband threshold forming quasi-

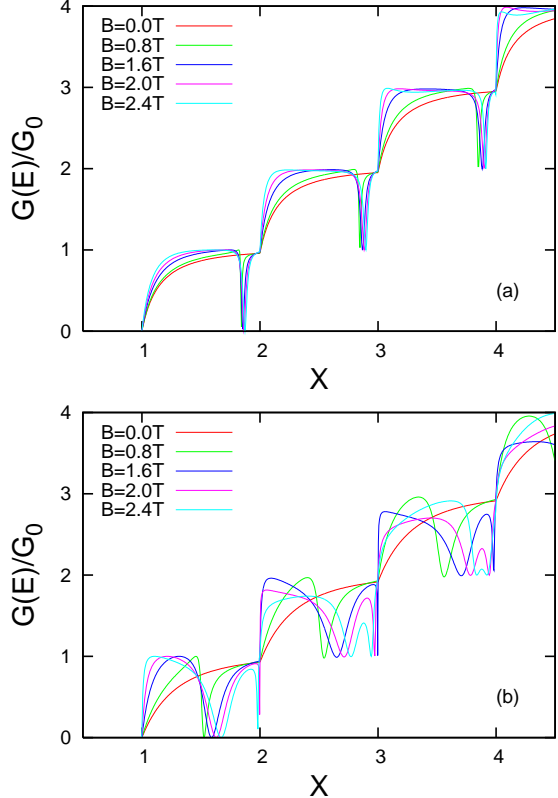


FIG. 3: Conductance of a parabolically confined wire as a function of the energy parameter  $X = E/\hbar\Omega_w + 1/2$  for various applied perpendicular magnetic fields. The amplitudes of the attractive impurity potential are (a)  $-6$  meV and (b)  $-12$  meV. Other parameters are  $\hbar\omega_0 = 6$  meV and  $\beta_2 a_w^2(B=0) = 1.897$ .

bound states.<sup>6</sup> It can be demonstrated that these quasi-bound states are formed in the leads out of the embedded Gaussian potential.<sup>14</sup>

For the case of strong attractive potential shown in Fig. 3(b), one can see that there are two types of quasi-bound state features. The mechanism of sharp dips below the subband threshold is similar to the case of weak attractive potential. On the other hand, it is interesting to see the valley structures in Fig. 3 for  $B \neq 0$ . These valleys correspond to quasi-bound states formed in the attractive Gaussian potential. When the applied magnetic field becomes stronger, the blue shift of these valleys indicates such quasi-bound states are formed closer to the edge of the Gaussian potential due to the cyclotron motion. The large width of these valley structures implies the short life time of these quasi-bound states. When increasing the strength of the magnetic field, these valleys become wider. This indicates that the electrons in high magnetic field with short cyclotron radius easily escape from the quasi-bound states formed in such a strong attractive potential. We note in passing that in the absence of magnetic field, the intersubband transition is forbidden since the attractive potential is uniform in the transverse

direction, and we cannot see any dip structures in  $G(E)$ .

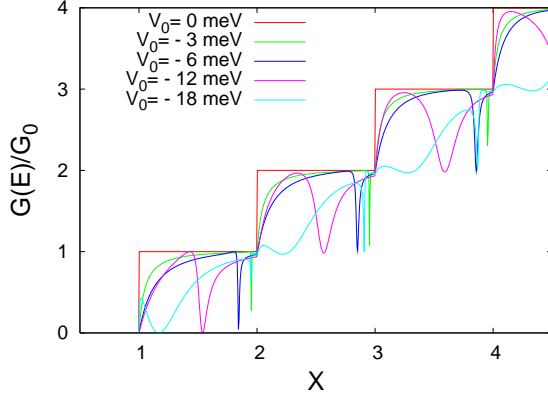


FIG. 4: Conductance of a parabolically confined wire as a function of incident electron energy for various amplitudes of attractive potential. The other parameters are taken to be  $B = 1$  T,  $\hbar\omega_0 = 6$  meV, and  $\beta_2 a_w^2(B = 0) = 1.897$ .

In Fig. 4, we study how the conductance can be affected by changing the amplitude of the attractive potential by fixing the strength of the magnetic field  $B = 1$  T, the confining potential  $\hbar\omega_y = 6$  meV, and the Gaussian parameter  $\beta_2 a_w^2(B = 0) = 1.897$ . In the absence of the Gaussian potential (red curve), the electron transport manifests an ideal quantized conductance, the magnetic field plays no role. When increasing the amplitude of the attractive potential, the subband levels in the potential will decrease in energy. Therefore, we can find a red shift of the quasi-bound states. More precisely, for the cases of  $V_0 = -3, -6, -12$ , and  $-18$  meV, the dip structures occur at around  $E/\hbar\Omega_w = 1.95, 1.84, 1.54$ , and  $1.17$ , respectively, in the attractive potential. It is also interesting to note that when the attractive potential is very strong, such as  $V_0 = -18$  meV, one can see a second dip structure appearing below the subband thresholds, both are quasi-bound states of the attractive potential.

Figure 5 shows the conductance as a function of incident electron energy for several values of magnetic field in the presence of a repulsive potential. The magnetic fields are tuned from 0 to 2.4 T for either weak ( $V_0 = 6$  meV) or strong ( $V_0 = 12$  meV) repulsive potentials, as shown in Fig. 5(a) and (b), respectively. For the case of weak repulsive potential shown in Fig. 5(a), one can see that the conductance plateaus are suppressed from the ideal case. When increasing the applied perpendicular magnetic field, the suppressed conductance plateaus tend to be enhanced back to the ideal case. For the case of strong repulsive potential (see Fig. 5(b)), the conductance curves are suppressed much more than those for the weak repulsive one. Without a magnetic field, the conductance behaves according to Ohm's law. When the applied magnetic field is increased, the conductance can be enhanced, and the quantization behavior becomes slowly recognizable.

One may want to see how the conductance can be af-

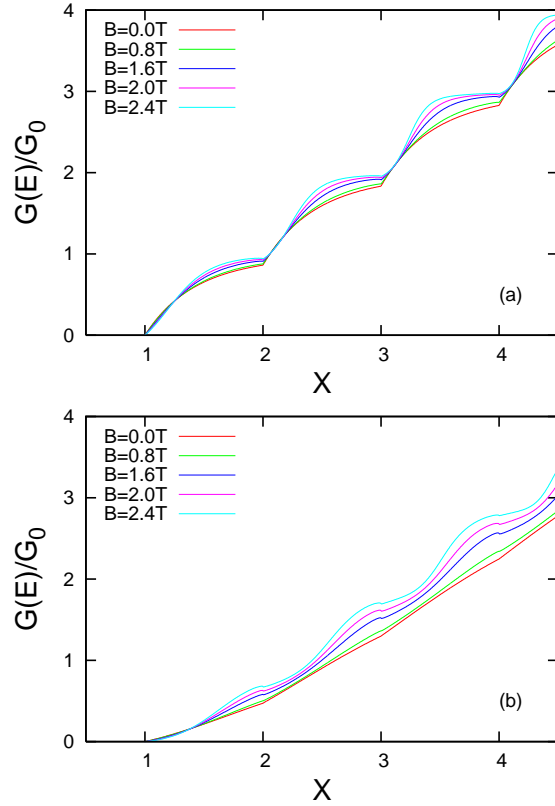


FIG. 5: Conductance as a function of incident electron energy with various applied magnetic fields. The amplitudes of the repulsive potential barrier are  $V_0 =$  (a)  $6$  meV and (b)  $12$  meV. Other parameters are  $\hbar\omega_0 = 6$  meV. and  $\beta_2 a_w^2(B = 0) = 1.897$ .

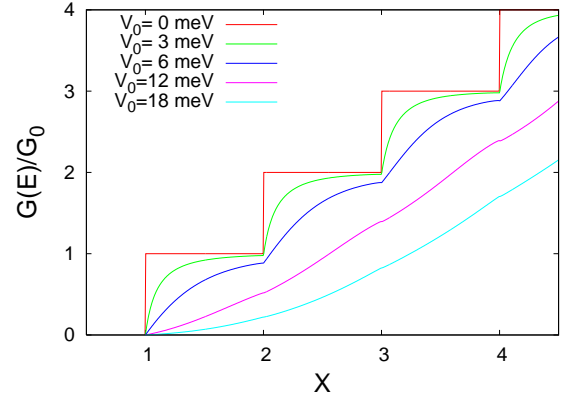


FIG. 6: Conductance as a function of incident electron energy with various amplitudes of repulsive potential. Other parameters are taken to be  $B = 1$  T,  $\hbar\omega_0 = 6$  meV, and  $\beta_2 a_w^2(B = 0) = 1.897$ .

fected by changing the amplitude of the repulsive potential, as is shown in Fig. 6. We fix the strength of the magnetic field  $B = 1$  T, the confining potential  $\hbar\omega_y = 6$  meV of the nanowire, and the potential configuration  $\beta_2 a_w^2(B = 0) = 1.897$ . In the absence of scattering

potential, the conductance is ideally quantized. When increasing the amplitude of the repulsive potential, the electrons are reflected by the barrier and the conductance is strongly suppressed. For weak barrier, such as  $V_0 = 3$  and  $6$  meV, the quantization behavior in  $G(E)$  is still visible. However, when the barrier is strong enough, such as  $V_0 = 12$ , and  $18$  meV, not only the conductance is strongly suppressed, but the quantization behavior in  $G(E)$  has vanished.

To conclude this section, we note in passing that when the scattering potential (well or barrier) is uniform in the transverse direction it does not break the translational invariance along the lateral confining direction. However, in the presence of magnetic field, if such a scattering potential is a well then one can find quasi-bound states due to elastic intersubband transitions to a higher subband threshold. However, if the scattering potential is a barrier, one finds no quasi-bound state features even in a magnetic field up to  $2.4$  T.

### B. Embedded quantum ring and dot

To model an embedded quantum ring with the parameterization (19) we initially choose the parameters used in Fig. 2, such that when  $B = 0$  then  $\beta_1 a_w^2 = 3.41$ ,  $\beta_2 a_w^2 = 11.37$ , and  $\hbar\Omega_w = 1.0$  meV. (The parameters of the potential (19),  $\beta_1$  and  $\beta_2$  do not depend on  $B$ , but  $a_w$  does).  $V_1 = -12$  meV, and  $V_2 = 18$  meV. We are thus investigating relatively broad wire with a small embedded ring structure with diameter of approximately  $40$  nm. We assume the wire to be a GaAs wire as mentioned above. The conductance (34) of the wire is presented in Fig. 7 for several values of the magnetic field. To compare the results for various values of the magnetic field it is convenient to observe the conductance as function of the energy of the incoming electron state scaled by the distance of the energy subbands, i.e.  $E/(\hbar\Omega_w) = E/E_w$  and furthermore use  $X = E/\hbar\Omega_w + 1/2$  such that an integral value of  $X$  indicates the number of incident modes.

In Fig. 7a we see that as soon as the magnetic field is different from zero a strong Fano-like<sup>15,16</sup> resonance dip appears in the first plateau just above  $X = 1.5$ . As we argue below the dip corresponds to a destructive quantum interference between a quasi-bound state in the ring and an in-state of the wire. Figure 8 displays the total probability to find an electron in the wire close to the scattering center, the quantum ring. The probability is calculated using the wave function (35) for two values of the energy of the incoming electron in the lowest transverse mode,  $n = 0$ . Just below the resonance at  $X = 1.4$  Fig. 8a reveals us a normal scattering process. The scattering only takes place very close to  $x \approx 0$  and on the left hand side we see the interference pattern for the incoming and the reflected wave. On the right hand side the electrons only travel in one transverse mode and only to the right so we have a constant probability already a short

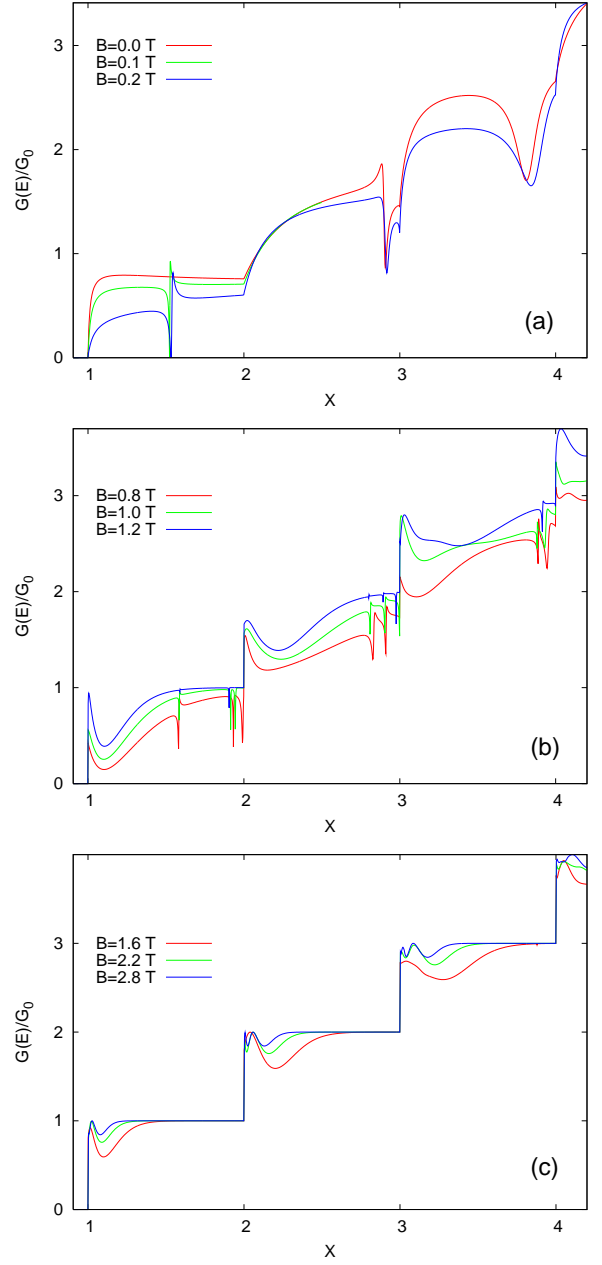


FIG. 7: The conductance of a parabolic wire with an embedded ring in units of  $G_0 = 2e^2/h$ .  $E_w = \hbar\Omega_w$ ,  $V_1 = -12$  meV,  $V_2 = 18$  meV,  $\hbar\Omega_0 = 1.0$  meV,  $\beta_1 a_w^2(B = 0) = 3.412$ ,  $\beta_2 a_w^2(B = 0) = 11.37$ , and 9 subbands are included.

distance away from the scattering center. The situation is quite different in Fig. 8b that displays the probability density for the state exactly in the resonance dip. Here no transmitted wave is present, but the probability close to the quantum ring is high enough that the probability for the incoming and the reflected waves is not visible on the color scale used.

The symmetry of the quasi-bound state indicates that it is an evanescent state belonging to the second subband  $n = 1$ . Without a magnetic field the scattering via the

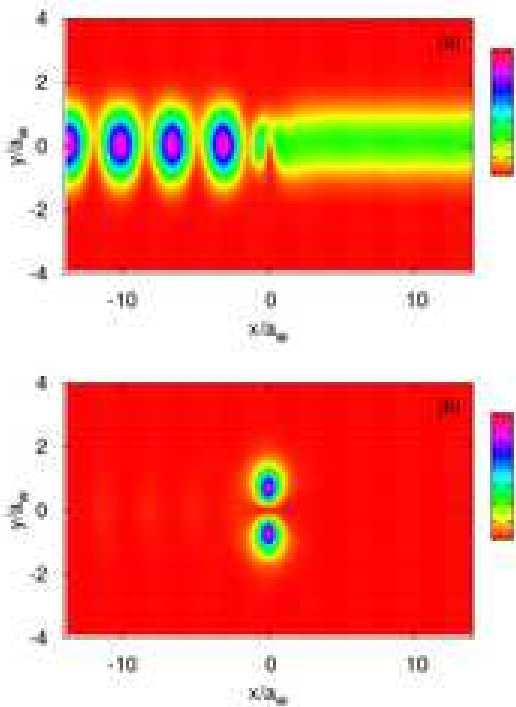


FIG. 8: The probability density of the scattering state  $\psi_E(x, y)$  in the parabolic quantum wire in the presence of an embedded quantum ring (Fig. 2), corresponding to the conductance in Fig. 7a at  $B = 0.1$  T. The incident energy  $X = 1.4$  (a), and  $X = 1.538$  (b) corresponding to the dip in the conductance.

evanescent state in the second subband is forbidden in the case of a symmetric potential placed in the middle of the wire. In that case a dip occurs in the second band due to a scattering through a evanescent state in the third subband.<sup>2,6,17</sup>

In order to further support our view that the resonance is due to a quasi-bound state of the quantum ring located in the continuum of the first subband (The ring lowers a state in the second subband into the first one), we see in Fig. 9a how the broadening or narrowing of the wire has little effects on the energy of the state. On the other hand, as seen in Fig. 9b the energy of the quasi-bound state changes linearly with the depth of the ring potential.

For some intermediate values of the magnetic field we see other minima occurring in the conductance closer to the end of the first step. For example, for  $B = 0.8$  T this is visible in Fig. 7b at  $X = 1.933$  and  $1.991$ . The corresponding probability densities are seen in Fig. 10. The symmetry of both densities indicates that the dips are caused by scattering via evanescent states of the second subband just as the dip in the middle of the first conductance step. These states are quasi-bound states of the ring further in the continuum of the first subband. The

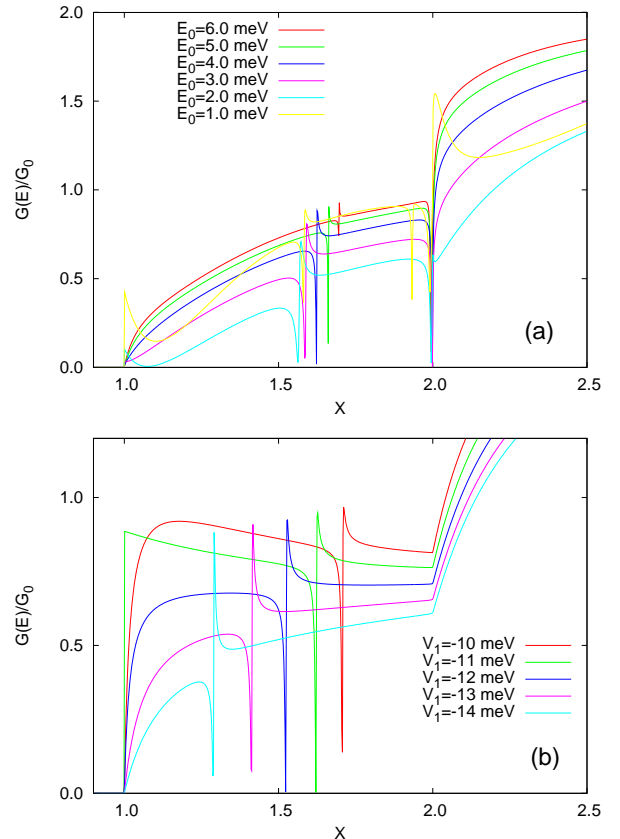


FIG. 9: The conductance of a parabolic wire with an embedded ring in units of  $G_0 = 2e^2/h$  as a function of the wire confinement  $E_0 = \hbar\Omega_0$  (a), and depth of the ring  $V_1$  (b).  $V_2 = 18$  meV,  $\beta_1 a_w^2(B = 0) = 3.412$ ,  $\beta_2 a_w^2(B = 0) = 11.37$ , and 9 subbands are included.  $E_w = \hbar\Omega_w$ ,  $B = 0.8$  T and  $V_1 = -12$  meV in (a).  $E_0 = 1.0$  meV and  $B = 0.1$  T in (b).

higher state, Fig. 10b has acquired more of the character of the geometry of the wire than the ring, and it extends far beyond the ring. The presence of Fano lineshapes in the conductance is not surprising as the mesoscopic Fano effect was already experimentally reported for both a single electron transistor<sup>18</sup> and an Aharonov-Bohm interferometer with an embedded quantum dot.<sup>19,20</sup> Nevertheless, in these two experiments the wire was much smaller than the mesoscopic system that caused the Fano interference. The results presented here suggest that this may be observed also in the case of a broad wire.

At still higher magnetic field, see Fig. 7c, the conductance has approached the ideal case as the magnetic field has now squeezed the wave functions together and closer to the edge as soon as the momentum is different from zero. The wave function thus bypasses the scattering potential. We shall see this effect clearer below.

The conductance of a wire with an embedded dot is presented in Fig. 11. The effects of an increasing magnetic field become very clear if we compare the probability density for the dips at  $X = 1.679$  when  $B = 0.6$  T, and the one at  $X = 1.557$  when  $B = 1.2$  T, see Fig. 12.

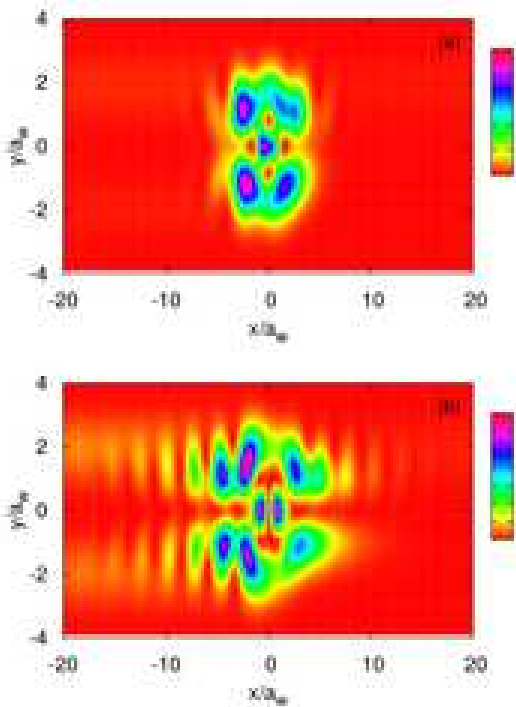


FIG. 10: The probability density of the scattering state  $\psi_E(x, y)$  in the parabolic quantum wire in the presence of an embedded quantum ring (Fig. 2), corresponding to the conductance in Fig. 7b at  $B = 0.8$  T. The incident energy  $X = 1.933$  (a), and  $X = 1.991$  (b), corresponding to two minima in the conductance at the end of the first step.

Both cases show a partial blocking of the channel due to backscattering caused by a quasi-bound state created by an evanescent state of the second subband, but the main difference is the total separation of the incoming and the reflected channel at the higher magnetic field. At the lower magnetic field we still see a interference pattern between these channels.

To explore further the scattering from the embedded dot when there is not a complete separation between the edge and bulk channels we show the probability density for  $X = 2.235$  at  $B = 0.6$  in Fig. 13. This energy corresponds to a dip seen in Fig. 11a. Due to the magnetic field and the scattering potential there is always a scattering between these two channels irrespective of whether the instate belongs to the  $n = 0$  (Fig. 13a) or the  $n = 1$  (Fig. 13b) mode. This is visible in the probability density with interference pattern in all channels.

The situation is completely different at the higher magnetic field  $B = 1.2$  T seen in Fig. 14. Here the same scaled energy as before,  $X = 2.235$ , corresponds to a peak in the conductance displayed in Fig. 11b. The value of the conductance peak indicates that there is very little backscattering. The edge channel ( $n = 0$ ) is almost entirely transmitted as Fig. 14a shows, but a quasi-bound

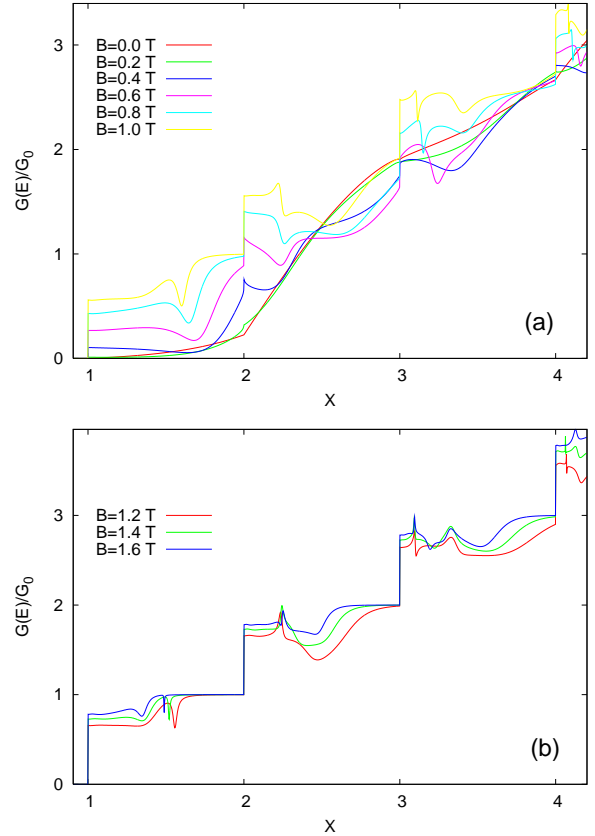


FIG. 11: The conductance of a parabolic wire with an embedded dot in units of  $G_0 = 2e^2/h$ .  $E_w = \hbar\Omega_w$ ,  $V_1 = 12$  meV,  $V_2 = -18$  meV,  $\hbar\Omega_0 = 1.0$  meV,  $\beta_1 a_w^2(B = 0) = 3.412$ ,  $\beta_2 a_w^2(B = 0) = 11.37$ , and 9 subbands are included.

state is seen in Fig. 14b belonging to the same subband as the instate.

The small quantum ring embedded in the broad wire (Fig. 2) is to small to show any indication of Aharonov-Bohm oscillations, and as the magnetic length gets smaller with increasing field strength the edge states bypass the ring. To change this situation we also did calculations for a larger ring shown in Fig. 15 compared to the smaller ring used in the preceeding calculations.

Of course the parabolic confinement of the wire always leads to the situation that at a high enough magnetic field the edge states will not be scattered by the quantum ring potential, but now at an intermediate field strength the magnetic length compares more favorably with the size scale of the ring as can be seen in the conductance displayed in Fig. 16 for both  $B = 0$  and 1 T. At  $B = 1$  T we see oscillations growing in wavelength with  $E$  or  $k_n(E)$  both for mode  $n = 0$  and 1.

The oscillations in the conductance at  $B = 1$  T are caused by a simple geometrical resonance where the wavelength of the scattering state in the ring has to compare appropriately with the circumference of the ring to build constructive or destructive interference, i. e. a Aharonov-Bohm like effect. This also explains the grow-

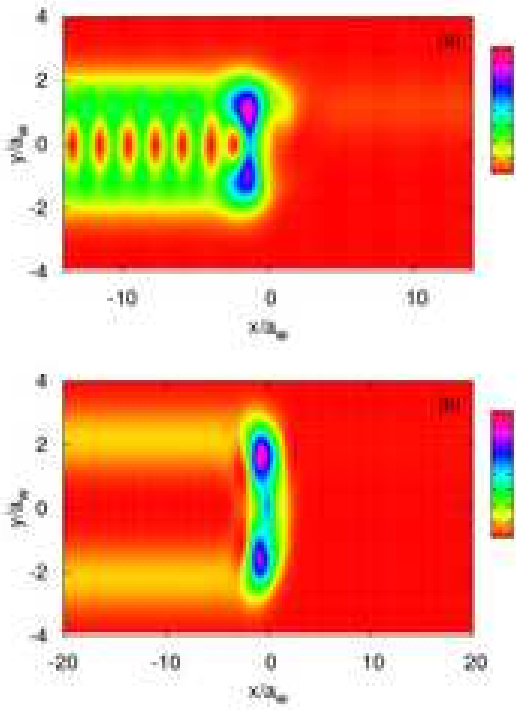


FIG. 12: The probability density of the scattering state  $\psi_E(x, y)$  in the parabolic quantum wire in the presence of an embedded quantum dot (Fig. 2), corresponding to the conductance in Fig. 11. The incident energy  $X = 1.679$  at  $B = 0.6$  T (a), and  $X = 1.557$  at  $B = 1.2$  T (b), corresponding to two minima in the conductance at the end of the first step.

ing wavelength of the oscillation with  $(E - E_0)$ . Even though the same condition lies at the root of the energy spectrum of stationary states in a ring in equilibrium we are not probing here the energy spectrum of the ring. We would like to mention that a similar oscillatory behavior of the conductance as a function of the energy was reported by Sivan et al.<sup>21</sup> in the case of a quantum dot in high magnetic field. Since in high magnetic field the cyclotron radius is smaller than the ring radius one expects the electrons to travel within the ring along skipping orbits before they leave through the wire.

The large size of the embedded ring in this case and its finite depth mean that quasi-bound states will not be of the same simple structure as seen for the smaller ring. This can be verified by the probability densities shown in Fig. 17 for the two dips at  $X = 1.319$  and  $1.347$ , and for the maximum at  $1.425$ . The total transmission of the only mode,  $n = 0$ , in Fig. 17c causes the perfect left-right symmetry, but the probability density in Fig. 17a corresponding to the dip at  $X = 1.319$  reflects the asymmetry caused by the confining parabolic potential to the ring seen in Fig. 15b. The structure of the evanescent states in Fig. 17a and b indicates that they are caused by states in the third and fifth energy bands and probably also

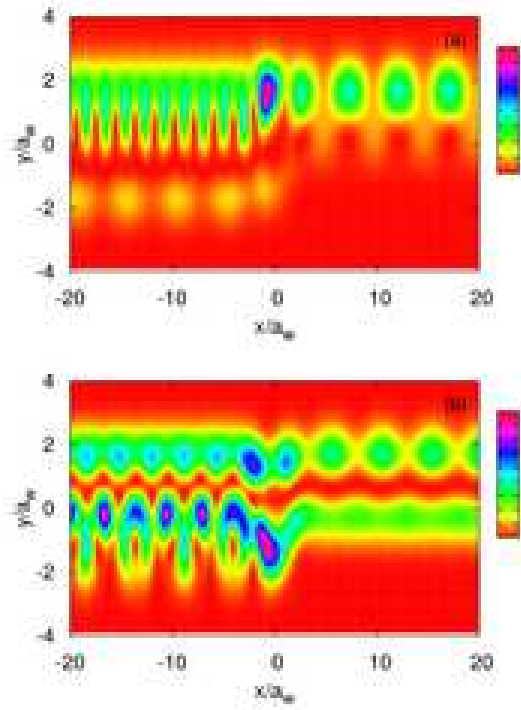


FIG. 13: The probability density of the scattering state  $\psi_E(x, y)$  in the parabolic quantum wire in the presence of an embedded quantum dot (Fig. 2), corresponding to the conductance in Fig. 11a at  $B = 0.6$  T for a state with incident energy  $X = 2.235$ , in mode  $n = 0$  (a), and  $n = 1$  (b).

states in higher bands. This persistence of eigenstates or scarring of wave functions in open systems has been discussed by Akis et al.<sup>22</sup> for quantum dots, and here we confirm it for an open quantum ring.

Superimposed on the Aharonov-Bohm like oscillations in the conductance in Fig. 16 we have narrow resonances that are caused by interaction with quasi-bound states of the ring. In Fig. 18a we show the probability density for the scattering state for an Aharonov-Bohm peak at  $X = 1.46$ . The density for a minimum in the oscillation is similar except for the addition of the reflected wave. In Fig. 18b we display the probability density for the first narrow resonance seen, at  $X = 1.135$ . Here we can identify a long lived evanescent state in the second subband.

#### IV. SUMMARY

We have successfully extended a multiband transport formalism build on the Lippmann-Schwinger equation in a magnetic field to be able to describe an unbiased transport through a broad wire with embedded small or large quantum dots and rings defined by a smooth potential. The calculation of the probability density for the scatter-

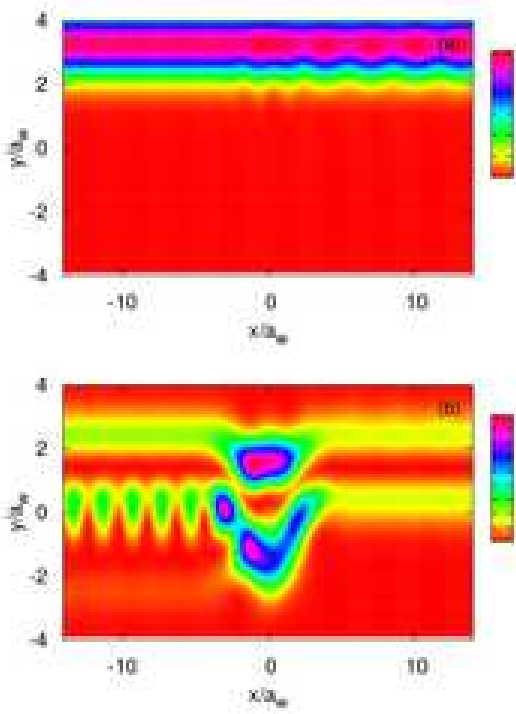


FIG. 14: The probability density of the scattering state  $\psi_E(x, y)$  in the parabolic quantum wire in the presence of an embedded quantum dot (Fig. 2), corresponding to the conductance in Fig. 11b at  $B = 1.2$  T for a state with incident energy  $X = 2.235$ , in mode  $n = 0$  (a), and  $n = 1$  (b).

ing states allows us to shed light on internal processes and resonances that in some cases reflect interaction between states in several subbands of the wire. We observe well known evanescent states and Fano resonances produced by these interactions. In the case of a large ring with finite width we observe Aharonov-Bohm type of oscillations superimposed with narrow resonances reflecting its energy spectrum.

Due to the wide range of system parameters used we had to pay extra attention to the accuracy of the numerical methods employed.

#### APPENDIX A: MATRIX ELEMENTS OF THE SCATTERING POTENTIAL

The matrix elements of the potential represented by a single Gaussian function  $V = V_0 \exp(-\beta_x x^2 - \beta_y y^2)$  is according to Eq.'s (25-26)

$$V_{nn'}(q, p) = V_0 a_w \sqrt{\frac{\pi}{\beta_x}} \exp\left[-\frac{(q-p)^2}{4\beta_x}\right] I_{nn'}(q, p), \quad (\text{A1})$$

where

$$I_{nn'}(q, p) = \int dy \phi_n^*(q, y) e^{-\beta_y y^2} \phi_{n'}(p, y). \quad (\text{A2})$$

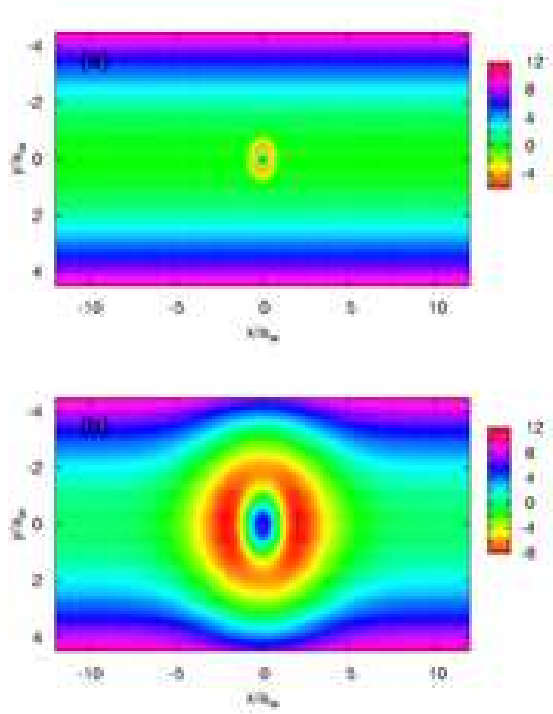


FIG. 15: A contour plot of the potential of an embedded quantum ring in wire. (a) a ring with  $\beta_1 a_w^2 = 3.41$ , and  $\beta_2 a_w^2 = 11.37$ , corresponding to the ring in the upper panel of Fig. 2. (b) a large ring with  $\beta_1 a_w^2 = 0.0682$  ( $B=0$ ), and  $\beta_2 a_w^2(B=0) = 0.682$ .  $E_0 = \hbar\Omega_w = 1.0$  meV,  $a_w = 33.7$  nm at  $B = 0$  T.

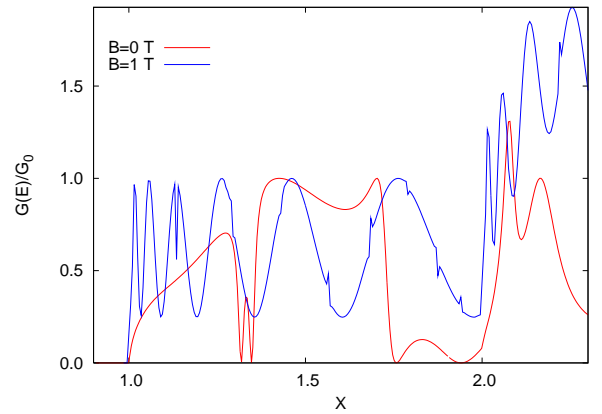


FIG. 16: The conductance of a parabolic wire with a large embedded ring (corresponding to Fig. 15b) in units of  $G_0 = 2e^2/h$ .  $E_w = \hbar\Omega_w$ ,  $V_1 = -12$  meV,  $V_2 = 18$  meV,  $\hbar\Omega_0 = 1.0$  meV,  $\beta_1 a_w^2(B=0) = 0.0682$ ,  $\beta_2 a_w^2(B=0) = 0.682$ , and 13 subbands are included.

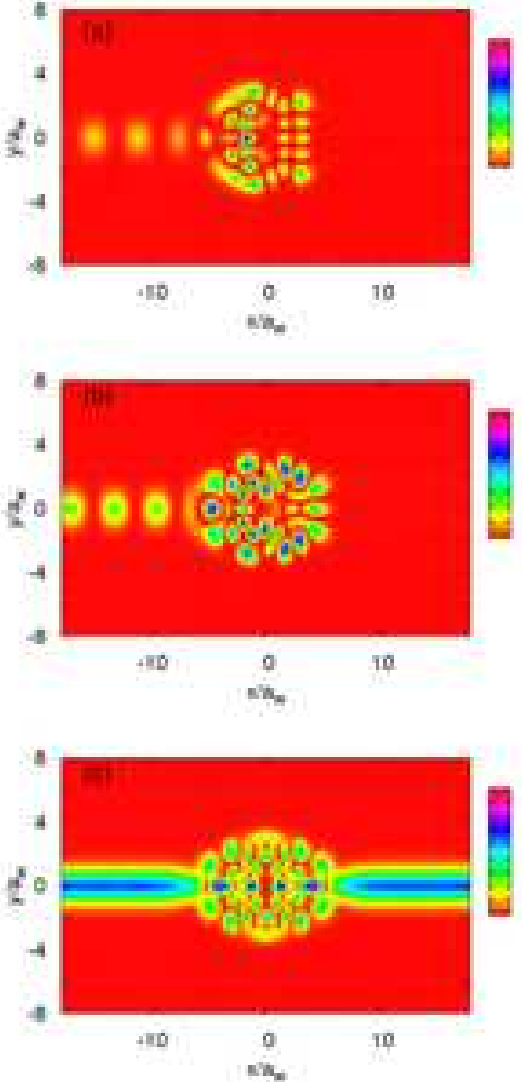


FIG. 17: The probability density of the scattering state  $\psi_E(x, y)$  in the parabolic quantum wire in the presence of an embedded large quantum ring (Fig. 15b), corresponding to the conductance in Fig. 16 at  $B = 0$  T for a state with incident energy  $X = 1.319$  corresponding to a dip (a),  $X = 1.347$  in a dip (b), and  $X = 1.425$  at a maximum (c). The incoming mode is  $n = 0$ .

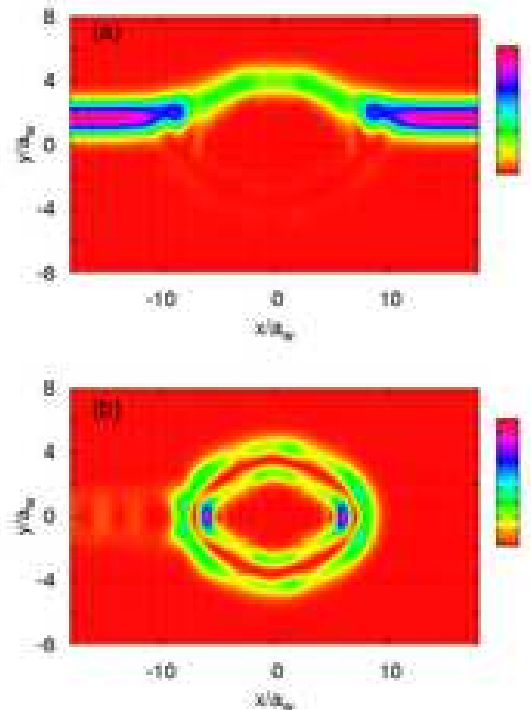


FIG. 18: The probability density of the scattering state  $\psi_E(x, y)$  in the parabolic quantum wire in the presence of an embedded large quantum ring (Fig. 15b), corresponding to the conductance in Fig. 16 at  $B = 1$  T for a state with incident energy  $X = 1.46$  corresponding to a peak (a),  $X = 1.135$  in a narrow dip (b). The incoming mode is  $n = 0$ .

Insertion of the expressions for the eigenfunctions (22) yields

$$\begin{aligned}
 I_{nn'}(q, p) = & \frac{\exp\left[\frac{(s_n+s_{n'})^2}{4C} - \frac{s_n^2+s_{n'}^2}{2}\right]}{2^{n+n'}\sqrt{Cn!n'!}} \\
 & \sum_{p=0}^n \sum_{q=0}^{n'} \binom{n}{p} \binom{n'}{q} H_p(-\sqrt{2}s_n) H_p(-\sqrt{2}s_{n'}) \\
 & \sum_{l=0}^{\min(n-p, n'-q)} 2^l l! \binom{n-p}{l} \binom{n'-q}{l} \\
 & b^{\frac{N}{2}-l} H_{N-2l} \left( z \sqrt{\frac{2}{bC}} \right), \tag{A3}
 \end{aligned}$$

where  $N = n + n' - p - q$ ,  $s_n = y_0^n = k_n a_w \omega_c / \Omega_w$ ,  $z = (s_n + s_{n'}) / (2\sqrt{C})$ ,  $C = (1 + \beta_y a_w^2)$ , and  $b = (1 - 2/C)$ . When the variable  $b$  assumes negative values the combination  $(\sqrt{b})^{N-2l} H_{N-2l}(\dots/\sqrt{b})$  still supplies the correct real value.

## ACKNOWLEDGMENTS

The research was partly funded by the Research and Instruments Funds of the Icelandic State, the Research Fund of the University of Iceland, and the National Sci-

ence Council of Taiwan. C.S.T. acknowledges the computational facility supported by the National Center for High-performance Computing of Taiwan. V.M. was supported by a NATO Science Fellowship.

---

<sup>1</sup> C. S. Chu and R. S. Sorbello, Phys. Rev. B **40**, 5941 (1989).

<sup>2</sup> P. F. Bagwell, Phys. Rev. B **41**, 10354 (1990).

<sup>3</sup> V. Vargiamidis and O. Valassiadis, J. Appl. Phys. **92**, 302 (2002).

<sup>4</sup> G. Cattapan and E. Maglione, Am. J. Phys. **71**, 903 (2003).

<sup>5</sup> J. Faist, P. Gueret, and H. Rothuizen, Phys. Rev. B **42**, 3217 (1990).

<sup>6</sup> J. H. Bardarson, I. Magnudottir, G. Gudmundsdottir, C.-S. Tang, A. Manolescu, and V. Gudmundsson, (cond-mat/0408435) (2004).

<sup>7</sup> S.-X. Qu and M. R. Geller, Phys. Rev. B **70**, 085414 (2004).

<sup>8</sup> Y. Takagaki and K. Ploog, Phys. Rev. B **51**, 7017 (1995).

<sup>9</sup> S. A. Gurvitz, Phys. Rev. B **51**, 7123 (1995).

<sup>10</sup> C. S. Tang and C. S. Chu, Physica B **292**, 127 (2000).

<sup>11</sup> J. H. Bardarson, Master's thesis, University of Iceland, <http://www.raunvis.hi.is/reports/2004/RH-09-2004.html> (2004).

<sup>12</sup> M. I. Haftel and F. Tabakin, Nuclear Physics A **158**, 1 (1970).

<sup>13</sup> R. H. Landau, *Quantum Mechanics II - A Second Course* in *Quantum Theory* (John Wiley & Sons, Inc, 1996), 2nd ed.

<sup>14</sup> C. S. Tang, Y. H. Tan, and C. S. Chu, Phys. Rev. B **67**, 205324 (2003).

<sup>15</sup> U. Fano, Phys. Rev. **124**, 1866 (1961).

<sup>16</sup> J. A. Simpson and U. Fano, Phys. Rev. Lett. **11**, 158 (1963).

<sup>17</sup> S. A. Gurvitz and Y. B. Levinson, Phys. Rev. B **47**, 10578 (1993).

<sup>18</sup> J. Göres, D. Goldhaber-Gordon, S. Heemeyer, and M. A. Kastner, Phys. Rev. B **62**, 2188 (2000).

<sup>19</sup> K. Kobayashi, H. Aikawa, S. Katsumoto, and Y. Iye, Phys. Rev. Lett. **88**, 256806 (2002).

<sup>20</sup> K. Kobayashi, H. Aikawa, S. Katsumoto, and Y. Iye, Phys. Rev. B **68**, 235304 (2003).

<sup>21</sup> U. Sivan, Y. Imry, and C. Hartzstein, Phys. Rev. B **39**, 1242 (1989).

<sup>22</sup> R. Akis, J. P. Bird, and D. K. Ferry, Appl. Phys. Lett. **81**, 129 (2002).